AIAA JOURNAL
Vol. 47, No. 1, January 2009

Geometric Installation and Deformation Effects in High-Lift Flows

J. W. van der Burg*
National Aerospace Laboratory/NLR, 1059 CM Amsterdam, The Netherlands
H. Freiherr von Geyr† and R. Heinrich†
DLR, German Aerospace Center, 38108 Braunschweig, Germany
P. Eliasson‡
Swedish Defence Research Agency (FOI), SE-164 90 Stockholm, Sweden
T. Delille§
Dassault Aviation, 92210 Saint Cloud, France
and
J. Krier¶
Ingenieurburo Dr. Kretzschmar (IBK),
D-90431 Nurnberg, Germany

DOI: 10.2514/1.34300

For a three-dimensional half-model high-lift configuration in a wind-tunnel environment, flow separation near maximum lift is influenced by the presence of geometric details. To examine the influence of these details, three computational fluid dynamics based studies are carried out. The objective is to examine the influence of pressure tube bundles, wind-tunnel walls and model mounting, and the effect of model deformation for a high-lift wind-tunnel half-model. Viscous flow computations for a high-lift configuration including pressure tubes and wind-tunnel walls (and model mounting) are performed. Experiences gathered with these flow computations are reported and comparisons to wind-tunnel experiments are made. Four methods are deployed in order to study aeroelastic effects, namely, a lifting surface based aeroelastic method and three fully coupled methods. Three structural models of a high-lift wing are developed. Experiences with three fully coupled methods are reported and benefits and shortcomings are identified. It is concluded that geometrical installation and deformation effects for a half-model high-lift wing in a wind-tunnel environment are significant. The mounting of the half-model has the most significant effect on the aerodynamic coefficients.

Nomenclature

C_D	=	drag coefficient
C_L	=	lift coefficient
$C_{L,\max}$	=	lift coefficient for maximum lift point
C_l	=	local lift coefficient
k	=	turbulent kinetic energy
L	=	reference length
l	=	turbulent length scale
M	=	Mach number
P_0	=	static pressure
q_∞	=	dynamic pressure
Re_L	=	Reynolds number on reference length L
T_0	=	static temperature
x, y, z	=	physical coordinates
α	=	angle of attack
$\alpha_{\max}$	=	angle of attack for maximum lift point
ε	=	turbulent dissipation
η	=	spanwise station

Presented as Paper 4297 at the 25th Applied Aerodynamics Conference, Miami, 25–28 June 2007; received 29 August 2007; accepted for publication 8 April 2008.

*Senior Scientist, Department of Flight Physics and Loads, Aerospace Vehicles Division, Anthony Fokkerweg 2; vdburg@nlr.nl. Member AIAA.
†Research Scientist, Institute of Aerodynamics and Flow Technology, Department of Transport Aircraft, Lilienthalplatz 7. Member AIAA.
‡Research Leader, Division of Defence and Security, Systems and Technology Computational Physics Department. Member AIAA.
§Senior Scientist, Advanced Aerodynamics, 78 quai Marcel Dassault.
¶Senior Consulting Engineer, Rehdorfer strasse 4.

I. Introduction

IMPROVEMENT of the maximum lift performance of a transport aircraft is an important driver for the design of a high-lift system [1,2]. Modern high-lift systems are geometrically complex and consist of leading- and trailing-edge devices and high bypass ratio nacelles mounted under the wing. A high-lift system may contain many geometric details such as flap elements, flap track fairings, slat elements, slat tracks, a nacelle, strakes, a beret-basque-pylon, and a slat horn. Extensive wind-tunnel campaigns [3–5] are conducted which show that geometric details do have a significant influence on the stall behavior of a high-lift wing. To improve low-speed performance at flight conditions it is necessary to get a good understanding of the aerodynamic properties and the maximum lift behavior of high-lift flow. The flow physics of a high-lift configuration near maximum lift are complex. Dominant flow phenomena influencing high-lift flow are transition, flow separation, confluence of wakes, and flow unsteadiness at poststall conditions. Laminar-turbulent transition plays an important role as well [5,6].

Wind-tunnel experiments under atmospheric and cryogenic conditions are carried out and computational fluid dynamics (CFD) tools are used to assess maximum lift and maximum lift behavior for realistic high-lift transport aircraft configurations [7,8]. The validation of the numerical design of a high-lift low-speed system is achieved with subscale (high-lift) aircraft models. The final low-speed performance is then derived by extrapolation [9]. Computational fluid dynamics tools are used to extrapolate wind-tunnel data to flight conditions. Therefore, it is necessary to carefully validate

these CFD tools to accurately assess lift and maximum lift in flight conditions.

A number of studies are conducted which are reported here that focus on the influence of geometric installation and deformation effects for a high-lift wing. For a high-lift landing configuration mounted in the low-speed wind tunnel (LSWT) at Airbus Bremen, a significant reduction in lift (near maximum lift) is observed when pressure tube bundles are included, see [10].

In the European transonic wind tunnel (ETW) a flight Reynolds number is achieved by cryogenic temperature and a high total pressure. For such a high Reynolds numbers condition a difference in experimental and computed lift up to 5% is found [11]. The difference in experimental and computed drag is even larger, up to 10%. These differences could be attributed to geometric effects, such as model deformation, the presence of pressure tube bundles, or a nonuniform oncoming flow due to the presence of wind-tunnel walls and model mounting.

The deformation of a high-lift wind-tunnel model and its wing components during cryogenic pressurized wind-tunnel measurements should receive attention. The geometric dimensions (e.g., chord, thickness) of key components such as slats and flaps are almost an order of magnitude smaller than the main wing element. Therefore, a slat or a flap can have locally a different deformation compared to the main wing element, which leads to changes in gap and overlap.

To understand the influence of geometric details on lift and maximum lift, three detailed CFD-based studies** are performed for a half-model of the KH3Y (high-lift wind-tunnel model) configuration. These studies focus on the influence of 1) pressure tube bundles on maximum lift behavior, 2) wind-tunnel walls and model mounting under atmospheric and cryogenic wind-tunnel conditions, and 3) model deformation under cryogenic wind-tunnel conditions. The objective is to capture and to assess the influence of individual geometric variations. A geometric variation is studied for the same turbulence model and for (approximately) the same grid settings. The influence of the turbulence model and the local grid resolution on high-lift flows has been studied elsewhere [12]. The best practice guidelines for grid resolution and turbulence modeling are employed to achieve accurate high-lift flow solutions.

The first CFD study requires the geometry modeling of the high-lift landing configuration including slat tracks and pressure tubes. Pressure tubes are needed in a wind-tunnel experiment to measure experimental pressures. The pressure tubes are mounted as bundles next to the slat tracks. Viscous flow computations for a high-lift configuration including slat tracks (brackets) are reported [13], but studies involving pressure tube bundles have not been reported before.

In the second CFD study the interior geometry of the wind-tunnel walls and model mounting is modeled. The presence of the wind-tunnel walls and model mounting will influence the aerodynamic coefficients. In wind-tunnel experiments, a balance is employed to measure the aerodynamic forces on the (high-lift) half-model. These forces are converted by means of correction formulas to free flight conditions. Comparison of the computed aerodynamic forces with wind-tunnel experimental results is made. Viscous flow computations for a high-lift configuration mounted in a wind-tunnel environment are reported before. For a high-lift trapezoidal wing mounted in a wind tunnel it is concluded that to achieve an accurate simulation the wind-tunnel geometry must be included in the computational model [14].

In the third study different aeroelastic methods are used to study the effect of high-lift wing deformation. A static aeroelastic study for a high-lift wing is performed using three fully coupled methods. Furthermore, a method is employed that derives the deformation from experimental pressures (which is based on a lifting surface method). In the fully coupled methods efficient algorithms are introduced to accommodate for the deformation of multiple high-lift wing elements (slat, flap). Part of the work is to gain experience with the aeroelastic methods and algorithms and to identify benefits and shortcomings. Only limited validation data are available which makes it hard to assess the accuracy.

Aeroelastic studies for a high-lift configuration were reported earlier. Chang et al. [15] report on an aeroelastic study for a geometrically complex high-lift configuration including slats, pylons, engines, flaps, and winglets. On the experimental side high-lift research is reported for a diamond wing high-lift model [16]. In this study the influence of dynamic pressure on the flap gap, overhang, and wing twist is studied. Van der Burg et al. [17] studied high-lift wing deformation using a noncalibrated structural model.

II. Influence of Pressure Tube Bundles

Pressure measurements for a high-lift configuration require pressure tabs on the movable parts (like slats and flaps). These pressure tabs are connected by pressure tubes to modules in the fuselage where the pressure values are converted to electric signals. Normally, the pressure tube bundles extend from the slat or flap to the main wing along the slat or flap tracks and continue into the fuselage. In most cases, slat tracks are too small to accommodate pressure tube bundles so that they have to be fixed outside the slat tracks; this is the case in this experimental campaign. In the calculations, the bundled pressure tubes are modeled in the form of a single tube of the same diameter (as the bundle). The bundles are illustrated in Fig. 1.

A CFD study is conducted to investigate the influence on the (maximum) lift behavior for a high-lift landing configuration at low Reynolds number conditions (LSWT). The flow conditions (in mean values) are $M = 0.174$, $Re_L = 1.34 \times 10^6$ with reference length $L = 0.34$ m. The CFD study focuses on the influence of pressure tube bundles on the aerodynamic characteristics with the flap and slat deployed corresponding to a landing configuration. The size of the computational grid without pressure tube bundles is approximately 17.1 million nodes. By adding the pressure tube bundles to the geometry, an extra 400,000 nodes are introduced in the computational grid. On the aerodynamic surfaces approximately 510,000 nodes are distributed.

The computed lift curves using the Spalart–Allmaras turbulence model are shown in Fig. 2. In the computations the influence of the pressure tube bundles is confirmed qualitatively. A significant reduction of (the computed) maximum lift is observed. When the pressure tube bundles are included, the lift loss is on the order of $\Delta C_L \approx 0.1$. In the computations the point of maximum lift is shifted $\Delta\alpha_{\max} = +2$ deg when the pressure bundles are included. However, with bundles the computed angle of attack of maximum lift $\alpha_{\max}$ is 5 deg larger than the experimental point of maximum lift.

It is concluded that the blockage effect of the pressure bundles must be considered when aiming at an accurate prediction of maximum lift. A better practical way in the experimental setup would be to include the pressure tubes inside the slat tracks (if possible) to avoid the blockage effect.

The change in the slope due to the pressure tubes of the computed lift curves is in qualitative agreement with the change in slope of the experimental lift curves. The decrease in slope of the computed lift curve with tubes is quantitatively too large. The main reason for this is the development of a flow separation at the sixth slat track for the configuration with pressure tube bundles, see also Fig. 3. The occurrence of this flow separation can be attributed to the presence of two pressure tube bundles left and right of the sixth slat track.

Figure 4 shows the behavior of the spanwise lift force distribution at increasing angles of attack. The observed kinks are introduced by the flap track fairings and slat tracks/pressure tubes. For both configurations a lift breakdown occurs on the main wing element at the location of the sixth slat track. With bundles, this flow separation is present for all computed angles of attack. Without bundles, this flow separation develops only close to maximum lift. The development of such a flow separation is found in the measurements, but the size of the flow separation is overpredicted in the flow

**The studies are conducted in Task 1.1 of the Eurolift II project which is carried out under Contract No. AST2-2004-502896 of the 6th Framework Programme of the European Commission. Partners involved in Task 1.1 of the Eurolift II project are Airbus-Germany, Dassault, DLR, NLR, FOI and IBK.

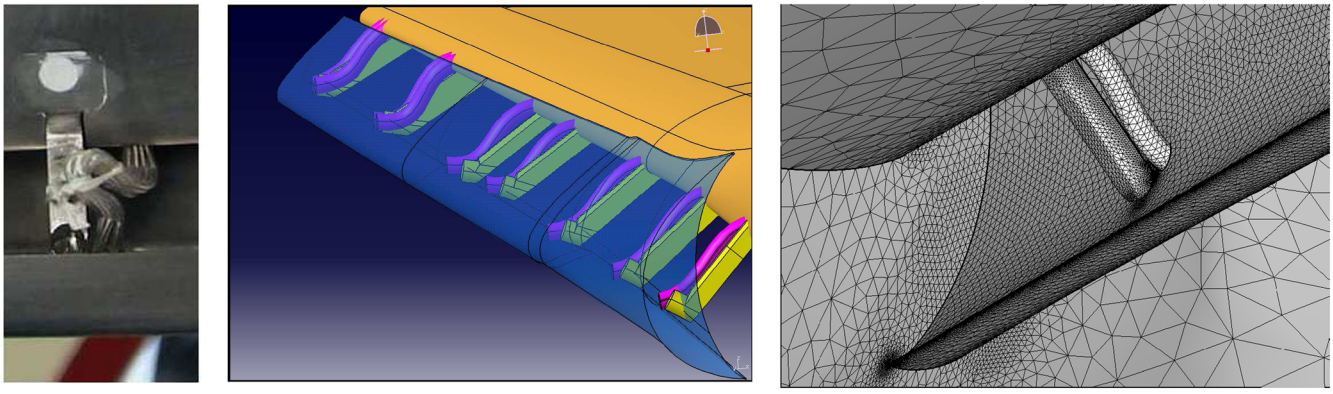

Fig. 1 The slat track and pressure tube bundles in a wind-tunnel setting (left), the computer aided design geometry model of the slat tracks and pressure tube bundles (middle), and a close-up of the triangular surface grid of a high-lift configuration at the slat cove (right). The slat track and the pressure tube bundle are modeled. The pressure tube bundle is modeled by a cylindrical displacement body.

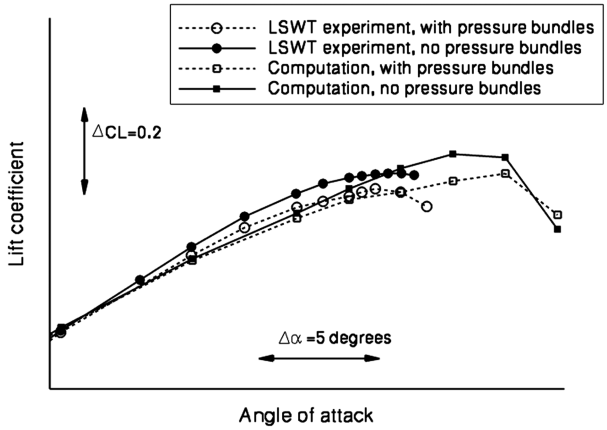

Fig. 2 Comparison of the computed and experimental lift curve for a high-lift configuration with slat tracks installed with and without pressure tube bundles installed.

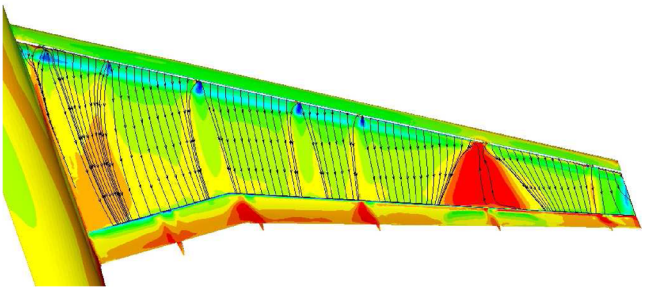

Fig. 3 Computed skin friction distribution for high-lift configuration with slat tracks and pressure tube bundles near maximum lift. The presence of slat tracks and pressure tube bundles introduces a blockage effect and induces vortical flow over the main wing element.

computations with bundles. As a consequence, larger drag coefficients are computed.

The reason for the overprediction in flow separation can be attributed to the dimensions of the cylindrical displacement body which may be too large in comparison to the pressure bundles used in the experiment. The size of the flow separation is also affected by the turbulence model and the amount of numerical dissipation.

III. Influence of Walls and Model Mounting in the Low-Speed Wind Tunnel

The LSWT wind tunnel consists of a 3-D nozzle, a closed test section, an open main circuit with the driving impeller (Eiffel type), and diffuser. The test section has a cross section of 2.1×2.1 m^2 and a length of 4.45 m. The half-model is mounted on the wind-tunnel ceiling as shown in Fig. 5. A boundary layer plate (model mounting) is inserted between the half-fuselage and the tunnel top wall and fixed to the tunnel wall turntable. Between the boundary layer plate and the half-fuselage a labyrinth seal is installed. The height of the model mounting including the labyrinth seal is 95 mm.

This study is reported in more detail in [18]. The model investigated is a takeoff configuration with a full span slat and a full span flap. The flap track fairings, slat tracks, and pressure tube bundles are not modeled. The flow conditions (in mean values) are $M = 0.174$, $Re_L = 1.34 \times 10^6$ ($L = 0.34$ m), $P_0 = 1006.3$ hPa; $T_0 = 25.8°$C. The values of Reynolds number, static pressure, and temperature vary slightly with the angle of attack.

The first step is to create a mesh including wind-tunnel walls and model mounting. The triangles in the corners of the wind tunnel are modeled as well. Figure 6 illustrates the computational grid of the high-lift configuration in the wind tunnel. The size of the in-tunnel computational grid is approximately 7 million grid nodes. The number of grid points on the model surface is 57,000. The number of points in the surface grid including the model with wind-tunnel walls and model mounting is 95,000. On the surface a structured type surface grid is employed that is decomposed in triangular cells. The number of the nodes on the model surface is relatively low since the grid is stretched in a spanwise direction, see also Fig. 6. In the wall normal direction 64 layers are created. A Delaunay based grid generation method is employed to fill the remaining part of the domain with tetrahedral elements.

Viscous flow computations are conducted using two different turbulence models, namely, a two-equation k–ε and k–kl explicit algebraic Reynolds stress model (EARSM) turbulence model. The k–ε two-equation turbulence model is equipped with a non-equilibrium correction [Menter shear stress transport (SST)] for a better prediction of flow separation.

Three angles of attack are calculated: one in the linear part of the lift curve, one at the point of maximum lift, and one in the stall zone. This requires the generation of three viscous meshes, one for each angle of attack. To stabilize the flow conditions it is necessary to increase the length of the tunnel at the entrance and at the exit. At the wind-tunnel entrance the density and velocity (flow rate) are imposed. At the exit a static pressure is imposed. The static pressure is adjusted at the exit to obtain the wind-tunnel conditions (Mach number and static pressure) at the test section. At the entrance a boundary layers thickness is imposed and adjusted to obtain the measured boundary layers thickness at the test section.

The computed lift curves for the in-tunnel results are shown in Fig. 7. The k–ε SST turbulence model gives results which are in agreement with the experimental lift curve until the point of maximum lift $\alpha_{\max}$. The k–kl EARSM turbulence model gives a somewhat better agreement with experimental lift in the poststall condition. The reason can be observed in Fig. 8. A large separated area has developed at the inboard part of the wing for the k–ε SST turbulence model, which is not present for the k–kl model.

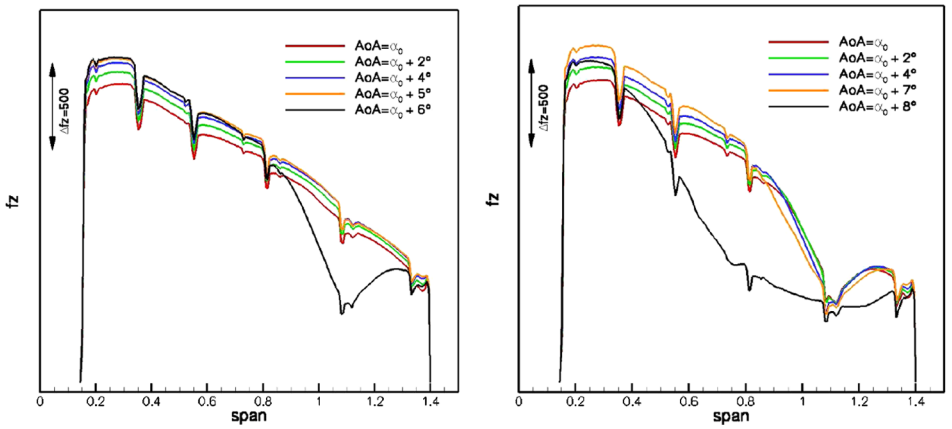

Fig. 4 Computed spanwise lift force distribution on the main wing element without (left) and with (right) pressure tube bundles. The computed spanwise lift force is shown for five increasing angles of attack (up to maximum lift) starting at $\alpha = \alpha_0$ in the linear range of the lift curve.

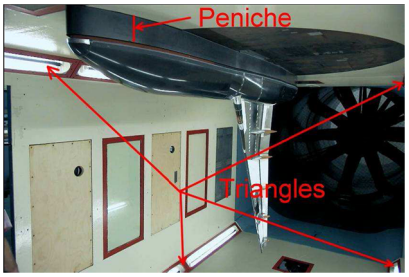

Fig. 5 KH3Y high-lift half-model mounted in the LSWT in Bremen.

The dominant stall mechanism computed with the *k–kl* EARSM turbulence model is a combination of slat separation, main wing trailing-edge separation, and inboard main wing separation. This stall behavior is similar for the free flight case. The lift coefficients computed for the free flight conditions underpredict the experimental lift coefficients, see Fig. 9. The point of maximum lift $\alpha_{\max}$ is correctly predicted.

To be able to understand differences between the in-tunnel result and the free flight result the normal velocity component at the plane of the model mounting height is plotted, see Fig. 10. This plane corresponds to the symmetry plane in the free flight case. It can be observed that for the in-tunnel computation nonzero normal velocity components exist at this location. The maximum value of the normal velocity is approximately 35% of the freestream velocity and occurs in the stagnation point. As a result of this the flowfield on the inboard high-lift wing is altered.

IV. Influence of Walls and Model Mounting in the European Transonic Wind Tunnel

A CFD study is conducted investigating the influence of wind-tunnel walls and model mounting on (maximum) lift for the KH3Y

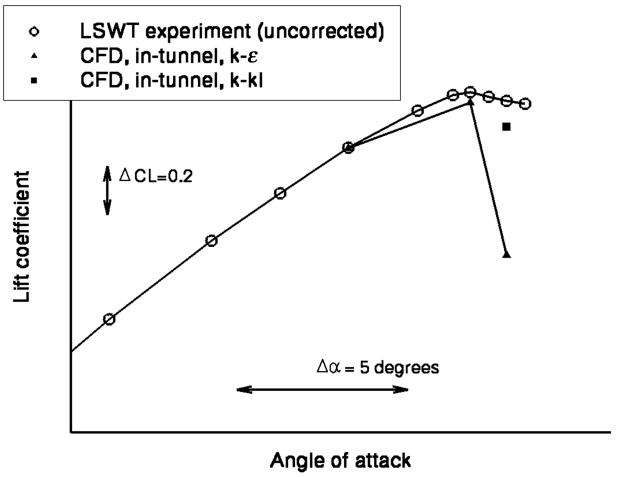

Fig. 7 Comparison of the lift coefficients for the computed in-tunnel CFD results with uncorrected LSWT experimental values.

half-model high-lift configuration that is mounted in the cryogenic wind tunnel ETW. The model investigated is a takeoff configuration with a full span slat and a full span flap identical to the model and setting in LSWT. The nacelle, flap track fairings, slat tracks, and pressure bundles are not modeled. The CFD study is reported in more detail in [19]. Similarly as in the LSWT study described in the preceding section, the wind-tunnel model is installed at the ceiling of the wind-tunnel wall using a model mounting, see Fig. 11. The flow conditions are $M = 0.177$, $Re_L = 15.1 \times 10^6$, and $L = 0.34$ m.

Similar to the LSWT in-tunnel computations, all wind-tunnel walls and the centerbody are modeled as viscous walls. A view of the surface grid is shown in Fig. 12. Three viscous grids are generated in the wind tunnel for three angles of attack, namely, one in the linear

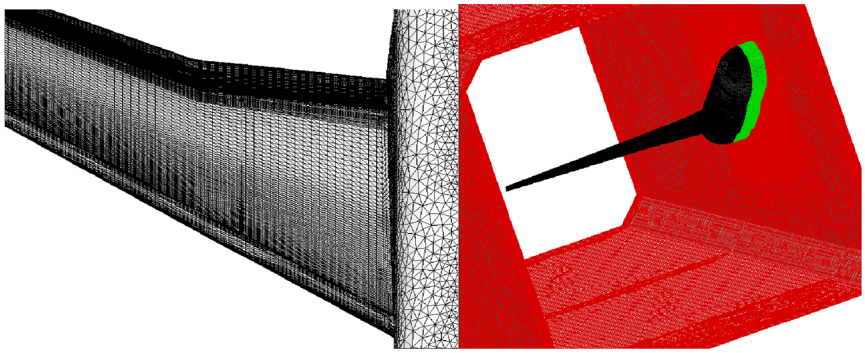

Fig. 6 Computational grid of the high-lift takeoff configuration without flap track fairings in the LSWT wind tunnel. In the surface grid of the high-lift wing spanwise stretching is adopted.

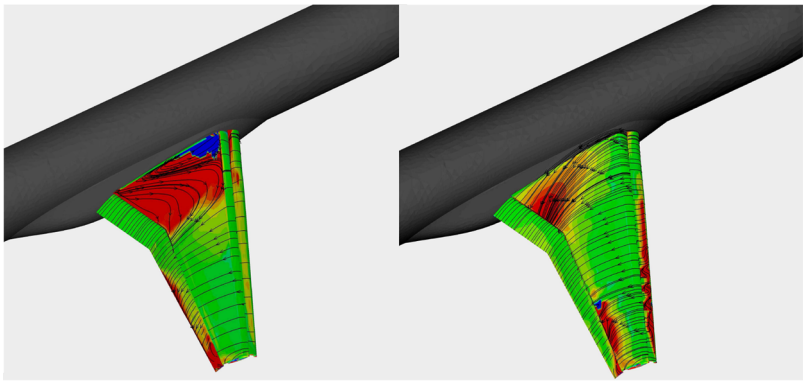

Fig. 8 Visualization of flow separation with skin friction lines of the in-tunnel flow computations near maximum lift with the k–ε SST turbulence model (left) and the k–kl EARSM turbulence model (right).

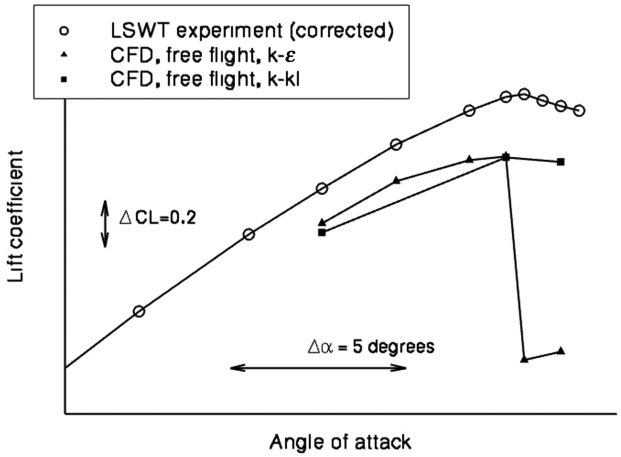

Fig. 9 Comparison of the lift coefficients for the computed free flight CFD results with corrected LSWT experimental values.

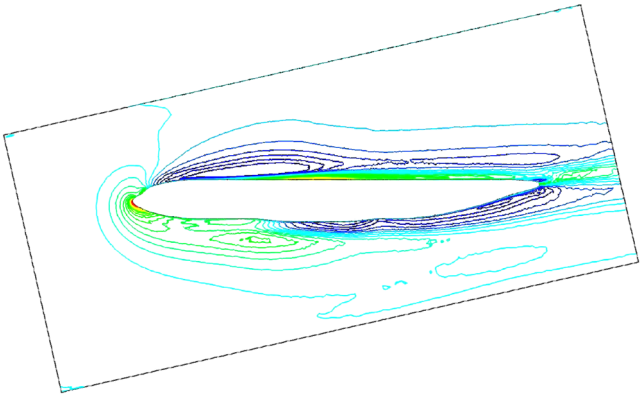

Fig. 10 Contours of the velocity component normal to the plane where the fuselage and model mounting are attached to each other. This plane corresponds to the symmetry plane in the free flight case. The high-lift half-model is mounted in LSWT.

range and two angles in the maximum lift region. The in-tunnel grids contain about 11 million grid nodes with about 200,000 nodes on the model surface. To reduce the number of grid nodes, grid stretching is introduced at the leading edges of the wing elements.

As in the LSWT computations the computational domain is extended far downstream with the intention to have uniform outflow so that a constant static pressure can be prescribed. This pressure, however, is not known a priori and needs to be determined.

An iterative algorithm is performed where the downstream pressure is varied to have a good match with available experimental

Fig. 11 ETW test section: the KH3Y half-model high-lift configuration mounted on the ceiling.

tunnel wall pressure distributions. This iterative algorithm is employed for all three computed angles of attack until a good match is obtained. In the flow computations an EARSM turbulence model is employed.

To allow comparison with free flight results, the numerical in-tunnel results are corrected to free flight using the same wind-tunnel correction formulas as employed for the ETW experimental data, see Fig. 13. Good agreement is obtained, in particular, from the in-tunnel calculations. Maximum lift is predicted at α_{max} which coincides with the experimental location. The level of the lift is well predicted for this angle; the drag is slightly underpredicted. Maximum lift in free flight is predicted approximately 1 deg later (compared to the corrected in-tunnel result) and the lift breakdown is less abrupt. The small underprediction in drag may be due to the absence of the flap track fairings in the calculations. At the highest angle of attack the flow is about to stall starting at the outer part of the wing. At this angle of attack the computations show an unsteady behavior and do not converge completely to a steady state. Average values of the forces are displayed here.

The difference between the corrected in-tunnel result and the free flight result can be understood by studying the flowfield in more detail. The in-tunnel results have a different velocity field at the inboard part close to the fuselage. On an inboard section this leads to a slightly lower pressure at the leading edge of the slat and main wing and a higher pressure at the rear main wing and flap. This corresponds to a small local change in the angle of attack and causes an overestimation of the drag force with about 10% in the free flight calculations compared to experimental and numerical in-tunnel results. Outboard, only small differences are observed.

The additional velocity causing the difference in pressure is due to crossflow components in the plane at a model mounting height observed in the in-tunnel computed results. In the vicinity of the stagnation point on the fuselage there is a large positive component

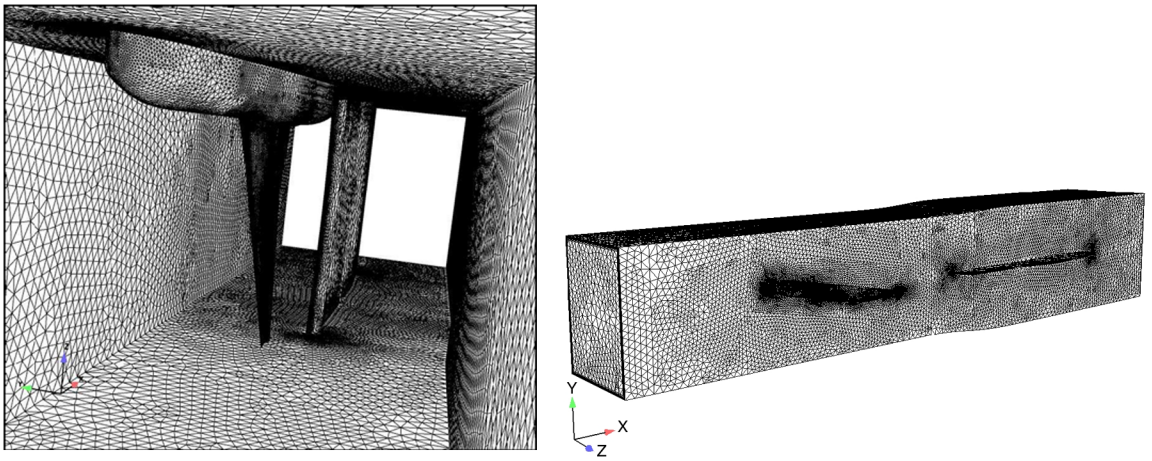

Fig. 12 View of the computational in-tunnel grid. Left: high-lift model mounted in the wind-tunnel ceiling with the centerbody in the background. Right: a view of the top wall where the model is mounted.

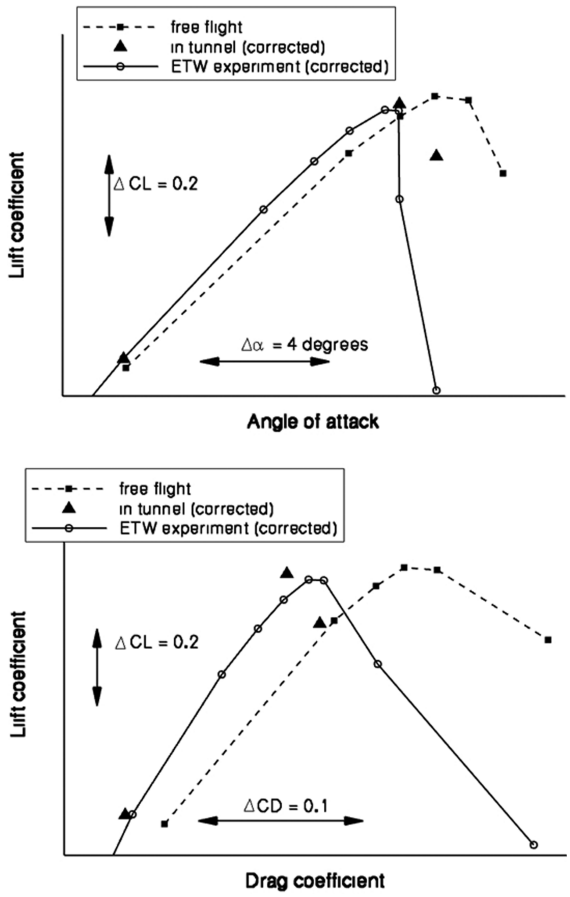

Fig. 13 Comparison of the computed lift curves and lift-drag curves for the free flight configuration with in-tunnel computations corrected to free flight and corrected experimental forces from ETW.

of the velocity normal to the plane that reaches up to about 50% of the freestream velocity, see Fig. 14. On top of the fuselage, on the other hand, there is a rather large negative velocity component. In fact, there are significant crossflow velocity components away from the model. These velocity components cause a redistribution of the inboard velocity field, pressure distribution, and forces. The fact that the flow is not parallel to this plane suggests that the mounting of the model can be improved. Opening the tunnel side wall slots may also remove some of these crossflow components.

Apart from the crossflow there is good agreement between the in-tunnel and free flight results. The pressure distributions agree well

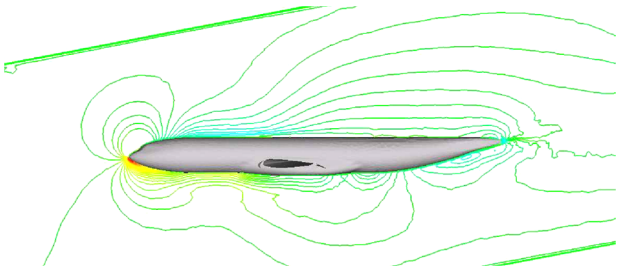

Fig. 14 Contours of velocity component normal to the plane where the fuselage and model mounting are attached to each other. This plane corresponds to the symmetry plane in the free flight case. The high-lift half-model is mounted in ETW.

from about 25% span out to the tip. This shows that the wind-tunnel corrections work correctly as intended.

At the highest angle of attack lift breakdown is obtained when computing inside the wind tunnel, whereas free flight computations give attached flow. Again, this is in better agreement with experimental results. Inspection of the stall behavior shows that a flow separation occurs at the outboard part of the slat at the leading edge. For the free flight case this separation is also present but less dominant in comparison to the in-tunnel separation. This indicates that the stall behavior is only moderately influenced by the presence of the wind-tunnel walls and model mounting.

V. Influence of Model Deformation

To achieve a high Reynolds number in the ETW wind tunnel a high dynamic pressure q_∞ is needed. Because of this high dynamic pressure the wing aerodynamically is highly loaded which causes the high-lift wind-tunnel model to deform. The flow conditions are $M = 0.177$, $q_\infty = 6.5$ kPa, $Re_L = 15.1 \times 10^6$, and $L = 0.34$ m.

The aeroelastic effect is studied by employing four methods, namely, a method that derives the deformation from the available experimental pressure measurements and three fully coupled methods. A high-lift takeoff configuration with a full span flap (no flap tracks and no slat tracks installed) and a high-lift configuration with flap track fairings are studied, see Fig. 15.

The first method uses the experimental pressure distributions as input to derive a deformed shape of the high-lift wing. In this method an optimization algorithm based on a lifting surface algorithm is adopted. In the optimization algorithm the (experimental) spanwise lift distribution is matched by changing the twist angle of the spanwise sections. This results in a deformed shape of the high-lift wing. The method is restricted to attached flow without substantial distortion of wing flow by a nacelle or winglets. A limitation is that the lifting surface algorithm can only be used in the linear part of the

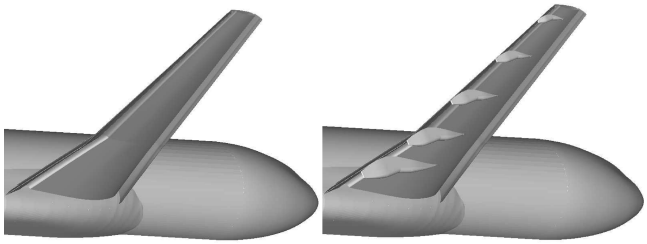

Fig. 15 Illustration of a high-lift configuration without flap track fairings (left) and a high-lift configuration with flap track fairings installed (right). The slat is deflected to 20 deg and the flap is set to 22 deg.

lift curve. For the rigid shape and the deformed shape an unstructured grid is generated and viscous flow computations are conducted to assess the effect of deformation.

Fully coupled methods are routinely used to study aeroelastic effects for instance of civil aircraft configurations at cruise conditions and military aircraft configurations at extreme maneuvering conditions. For a high-lift wing a static aeroelastic analysis using a fully coupled method is more challenging due to the existence of multiple (deforming) wing elements.

The starting point for a fully coupled computation is a computed viscous flow solution on a hybrid grid for the rigid shape. The deformation of the high-lift wing elements is computed based on the exerted aerodynamic forces. Local interpolation algorithms are employed to transfer forces to the structural grid and to transfer deformations (from the structural grid) to the aerodynamic surface grid.

The next step is the deformation of the three-dimensional unstructured hybrid grid. The prismatic part is deformed based on the computed local deformation of the aerodynamic surface. Highly efficient algebraic algorithms [20–22] are introduced for the deformation of a tetrahedral grid. These algebraic algorithms are a necessity for a high-lift configuration. The computational time for the algebraic algorithm [21] is on the order of a couple of minutes for a tetrahedral grid having 7 million nodes.

The deformed hybrid grid is preprocessed to obtain a deformed dual grid, and on this dual grid a fixed number of flow solver steps are taken (on the order of 100 Runge–Kutta time steps). The aeroelastic loop is repeated until the deformed shape is sufficiently converged. For the fully coupled methods a limited number of deformation steps are needed to reach a converged deformed high-lift wing. On the order of 10–15 deformation steps are taken.

VI. Structural Models

In the fully coupled methods a structural model is needed. To withstand the cryogenic temperatures and dynamic pressures, wind-tunnel models for the ETW are made out of steel (ASTM 579). The wind-tunnel model is not solid due to the need to install wind-tunnel instrumentation such as, for instance, pressure tubes.

Three structural models for the KH3Y wind-tunnel model are developed to represent the structure of the high-lift wind-tunnel model. Two high-order and one low-order structural models are developed. Table 1 gives an overview of these models and Fig. 16 displays two of the structural models.

In the computational structural mechanics (CSM) models the slat tracks and flap track fairings are modeled by means of three-dimensional elements (bricks or tets). The number of structural nodes in the tetrahedral based structural model is larger than the number of structural nodes in the CSM model based on bricks. This is understandable because in general more tetrahedral elements are needed to achieve comparable accuracy with a CSM model made of bricks.

Table 1 Overview of structural models developed for the high-lift wing

Model type	Structural nodes	Element type	Slat/flap tracks modeled
Flat plate	176	Plate	Yes
CSM	12,000	Bricks	Yes
CSM	90,000	Tets	Yes

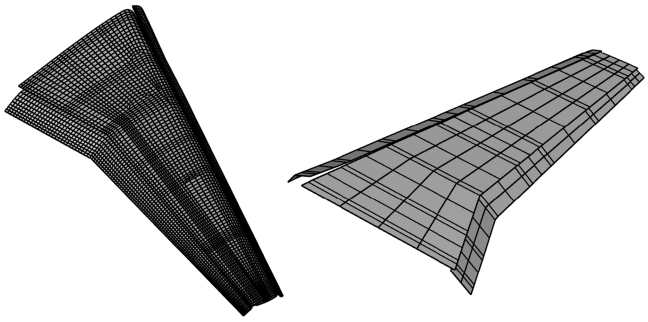

Fig. 16 Structural models developed for a high-lift wing: CSM model based on bricks (left) and a flat plate structural model (right).

The holes inside the main wing are not modeled in the CSM models. The influence of holes inside the main wing element on the overall stiffness of the high-lift wing is relatively small. This is verified in a sensitivity study using the CSM model based on tetrahedral elements. Furthermore, because the ETW balance is relatively stiff, a negligible effect on deformation is expected and hence the stiffness of the balance is not accounted for.

The low-order structural model is based on two-dimensional plate elements and consists of a limited number of structural nodes. This model is developed to examine the feasibility to achieve a short computational turnaround time. The high-lift wing elements are represented by plate elements. The stiffness of the main wing element is constructed by assuming a piecewise constant wing thickness distribution using four spanwise groups of elements. The curvature of the slat is modeled by introducing a kink in the spanwise direction, see Fig. 16.

To support the validation of the structural models DLR conducted a static test of the wind-tunnel model. In this static test the slats and flaps are set to the landing position. The inboard flap is removed (not mounted) to avoid damage to the model. A load range from 0 to 800 N in steps of 100 N is applied to the main wing tip. Displacements are measured with an optical measurement system on the slat, wing, and flap. In total 45 measurement points are used. In the static test the bending of the main wing element is assessed.

The three structural models are validated for wing bending using this static test data. For the CSM models the Young modulus is tuned, so that the computed bending based on a CSM model agrees with the bending of the high-lift wing of the wind-tunnel model. Because three-dimensional elements are used it may be assumed that the CSM models represent wing twist appropriately as well. In the structural model based on plate elements the thickness of the (four) individual spanwise groups of elements is chosen, so that the computed bending matches the measured wing bending in the static test.

VII. Results

For the high-lift configuration without flap track fairings two aeroelastic methods are employed, namely, a method where the deformation is derived from the experimental pressures and a fully coupled method based on CSM tetrahedral elements. Denote the aeroelastic methods A and B, respectively. Different aerodynamic hybrid grids are defined for these methods. The size of the grids is on the order of 11.5 million grid nodes. Special care is taken to refine leading and trailing edges of the high-lift wing elements. In the flow computations the Spalart–Allmaras turbulence model is used for both methods.

In Fig. 17 the aeroelastic effect is illustrated. At $\alpha = \alpha_1$ deg the difference between the computed lift coefficients for the rigid and the deformed shape is 2% (for both methods). This corresponds to a reduction in lift coefficient of about $\Delta C_L \approx 0.04$. For method A at the lowest computed angle of attack a somewhat larger reduction in lift coefficient is computed, approximately 3%.

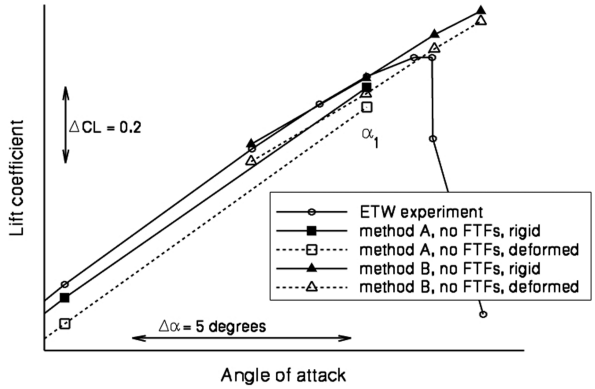

Fig. 17 Overview of the computed lift curves in the aeroelastic computations for a high-lift configuration without flap track fairings (FTFs). Two methods are employed, namely, a method where the deformations are derived from experiment (method A) and a method based on CSM tetrahedral elements (method B). The result on the undeformed (rigid) grid is shown as a solid line, whereas the result on the deformed grid is shown as a dashed line. The angle α_1 is introduced to link this figure to Fig. 20.

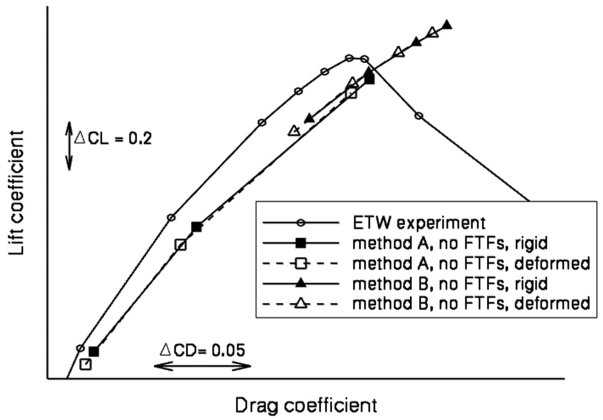

Fig. 18 Lift-drag curves computed using methods A and B compared to experimental values.

In Fig. 18 it can be observed (for methods A and B) that due to aeroelastic effect both the lift coefficient and drag coefficient reduce. The aeroelastic effect can be interpreted as a reduction in angle of attack of approximately $\Delta\alpha = -0.5$ deg.

The computed lift coefficients on the rigid for method B show a good agreement with the experimental lift curve. Inspection of the lift-to-drag curve shows that the drag coefficient is overpredicted by 10% at $\alpha = \alpha_1$ (method B), see Fig. 18. The computations illustrate that at this Reynolds number condition an aeroelastic effect is present. As shown before the effect of wind-tunnel walls is more significant, see also Fig. 13.

The difference in the lift coefficients computed on the rigid grids between methods A and B at $\alpha = \alpha_1$ is likely due to differences in grid and flow solver settings. The experimental point of maximum lift is overpredicted for method B on the rigid grid. The computed point of maximum lift is not yet reached. The same observations hold for the computed results on the deformed grid (for method B).

Another static aeroelastic study for the high-lift configuration with flap track fairings is conducted with the method using the CSM model based on bricks and the method using the flat plate structural model. The two methods are denoted as C and D, respectively.

For methods C and D the same computational grid is used, see Fig. 19. Spanwise stretching is introduced at leading edges of the high-lift wing elements to reduce the number of grid nodes. Grid stretching is allowed because no large gradients in the spanwise direction are expected at these locations. The resulting grid has approximately 7 million nodes with 146,000 nodes on the model surface. An isotropic grid using the same grid settings would result

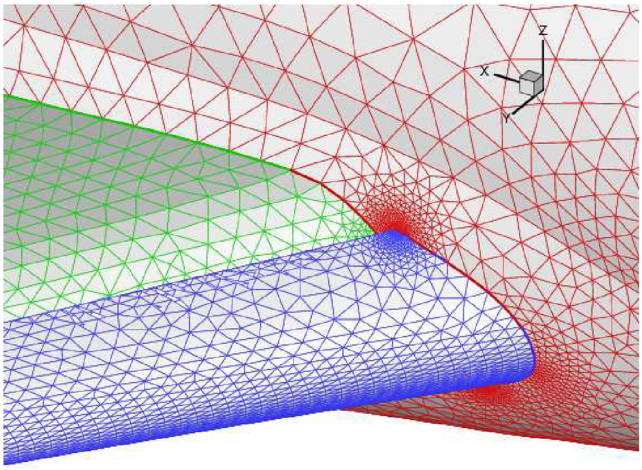

Fig. 19 Surface grid of the rigid high-lift configuration where grid stretching in the spanwise direction is employed. Structured surface triangles are introduced at the leading edge of the slat.

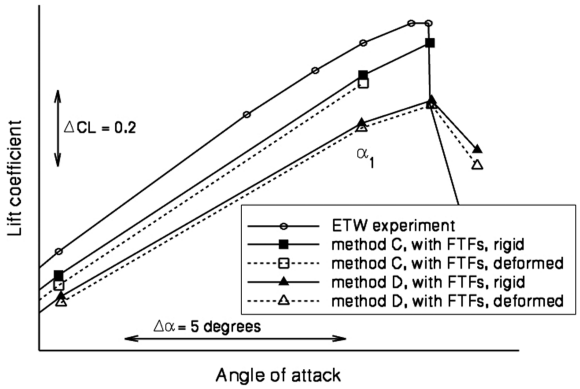

Fig. 20 Overview of the computed lift curves in the aeroelastic computations for a high-lift configuration with FTFs included. The results for a method using a CSM model based on brick elements (method C) and a method based on the flat plate model are compared. The result on the rigid grid is shown as a solid line, whereas the computation on the deformed grid is shown as a dashed line. The symbol α_1 is included to identify the same angle of attack as shown in Fig. 17.

on the order of 12 million nodes. Structured cells are introduced at the leading-edge wing elements [23,24].

The same flow solver is used; The Spalart–Allmaras turbulence model is adopted. In Fig. 20 it can be observed that the aeroelastic effect leads to a small reduction in lift for both methods. At angle of attack $\alpha = \alpha_1$ the reduction in lift coefficient is within 1% for both methods. This corresponds to a reduction in lift coefficient of about $\Delta C_L \approx 0.02$ for this angle of attack. The aeroelastic effect reduces both the lift coefficient and the drag coefficient. Similarly as for the high-lift configuration without flap track fairings, this can be interpreted as a reduction of the angle of attack. The estimated reduction in angle of attack for the configuration with flap track fairings is on the order of 0.25 deg (for both methods C and D). The computed effect with flap track fairings is smaller compared to the computed result without fairings.

The large difference in the computed lift coefficient on the rigid grid is due to a different flow solver setting. In method D a central scheme is employed to compute the aerodynamic coefficients. In method C matrix dissipation in combination with a preconditioning algorithm [25] is applied. Method C gives a significant larger computed lift coefficient, namely, $\Delta C_L = +0.12$ at $\alpha = \alpha_1$.

The computed lift for method C significantly underpredicts experimental lift for all angles of attack. This may (partly) be attributed to the presence of the flap track fairings. The effect of the flap track fairings is assessed by comparing the computed lift

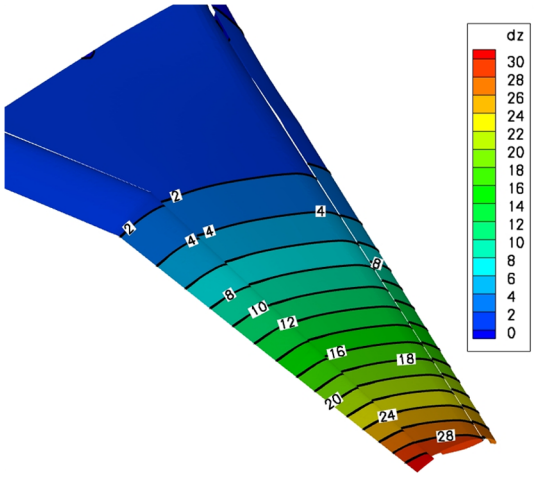

Fig. 21 Illustration of the computed deformation in the z direction (in mm) of high-lift wing configuration with flap track fairings installed resulting from the fully coupled aeroelastic computation based on bricks (method C). The flap track fairings are not displayed.

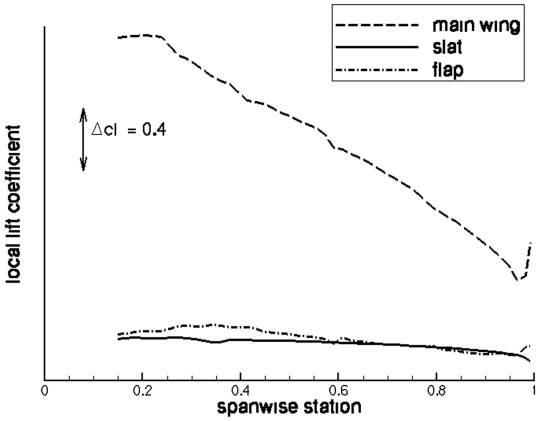

Fig. 22 Spanwise local lift distribution for the main wing, slat, and flap on the rigid grid at $\alpha = \alpha_1$ for method C. The flap track fairings are located at spanwise stations $\eta = 0.25$, 0.4, 0.58, 0.77, and 0.95.

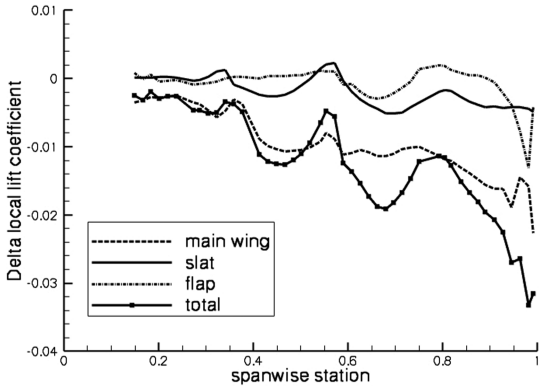

Fig. 23 The difference in computed local lift coefficients between the deformed grid and the rigid grid at $\alpha = \alpha_1$ for method C. The difference per wing component (main wing, slat, and flap) is shown and the total difference is displayed.

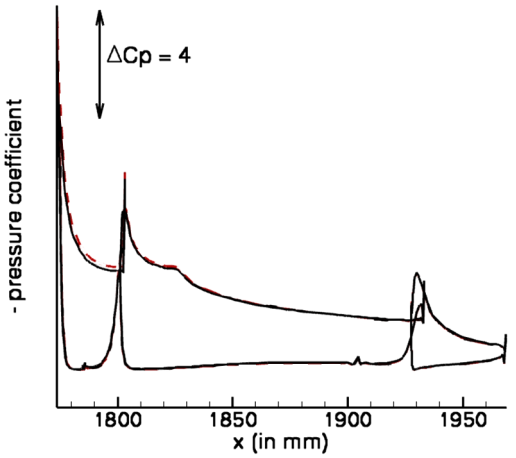

Fig. 24 Computed pressure coefficient distributions at outer wing section $\eta = 0.89$ plotted on the rigid grid for a high-lift wing configuration with flap track fairings (method C). The result computed on the rigid grid is displayed as a dashed line and the result on the deformed grid is shown as a solid line.

coefficient on the rigid grid for methods B and C at $\alpha = \alpha_1$ deg. The lift coefficient reduces with $\Delta C_L \approx 0.076$ which corresponds to a reduction in lift coefficient of approximately 3%. The reduction in lift can not only be attributed to the presence of flap track fairings; other effects such as different grid settings or flow solver settings could play a role here.

The computed aeroelastic deformation is shown in Fig. 21. A linear deformation of the high-lift wing is observed with the largest deformations occurring near the wing tip. The linear deformation can be interpreted as a bending and a twist of the wing around the aeroelastic axis (defined at 25% chord of the main wing element). The computed maximum wing deformation is approximately 30 mm which represents about 2% of the span width. The outer wing sections experience a nose down twist which can be interpreted as a reduction in the angle of attack. The inner part of the high-lift wing is clamped (in the structural model) and hence does not deform.

Figure 22 shows the computed spanwise lift distribution for the rigid high-lift configuration for method C. The aeroelastic effect reduces the sectional local lift on the high-lift wing, see Fig. 23. Near the tip region the reduction in local lift coefficient is on the order of $\Delta C_l \approx -0.03$. Near the wing root the reduction in local lift is relatively small. It can be observed in Fig. 23 that the loss in local lift can be attributed to the loss in lift of the main wing.

Figure 24 shows the computed chordwise pressure distribution at the outer wing section $\eta = 0.89$. The pressure coefficients at the leading edges of the slat and main wing element are slightly increased. The computed pressure coefficients at an inboard high-lift wing section do not change significantly.

For method D the point of maximum lift is computed at the same angle of attack as in the experiment (see Fig. 20). The stall behavior computed on the rigid grid is a leading-edge slat stall that induces a flow separation on the main wing element (see also [11]). In the fully coupled computation it is observed that the computed stall behavior does not change significantly. Beyond maximum lift the flow becomes unsteady which triggers a dynamic fluid-structure interaction.

In Fig. 25 the computed and measured spanwise wing bending and twist are compared. In the ETW experiment [4] the dynamic pressure is approximately 10% larger than in the flow computation. The computed bending and twist qualitatively agree to the experimental wing bending and twist. The maximum computed bending is found at the wing tip. The maximum computed wing bending is approximately 30 mm. The maximum computed wing twist is -1.0 deg at the wing tip. In the experiment somewhat smaller values for the wing bending and twist are found due to the larger dynamic pressure. The maximum computed twist using method A (twist is derived from the experimental lift distribution) is on the order of -1.2 deg.

The change in slat-gap height and wing-slat overlap can be observed in Fig. 26. The increase in slat-gap height due to deformation is approximately 0.7 mm at spanwise location $y = 950$ mm ($\eta = 0.68$). The increase is relatively large, on the order of 21%. The increase in overlap is approximately 0.5 mm at spanwise location $y = 950$ mm, which represents a change of 16%. At the location of the slat tracks the change in slat-gap height is zero. The

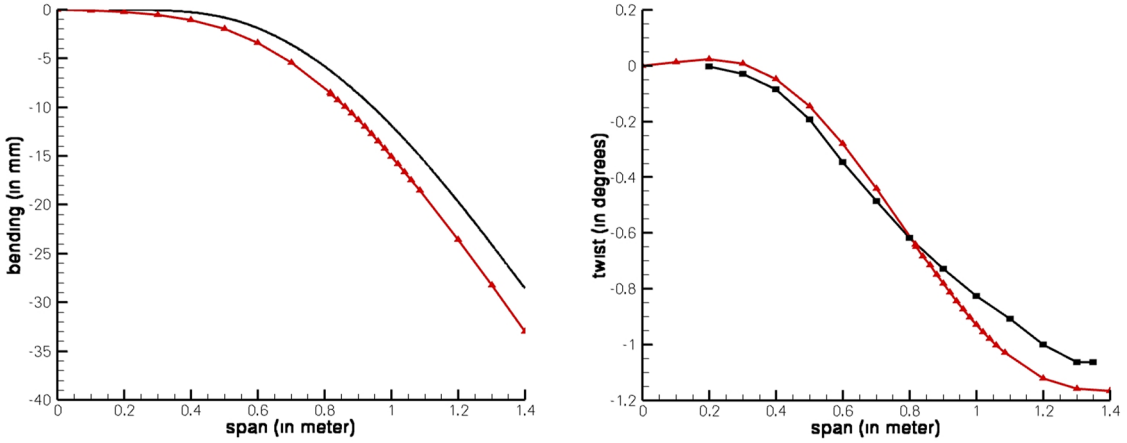

Fig. 25 Comparison of the computed and measured (lines with triangles) spanwise wing bending and twist at angle of attack $\alpha = \alpha_1$. In the flow computation (method C) the dynamic pressure is $q = 6.5$ kPa. In the ETW experiment the dynamic pressure is $q = 7$ kPa. A nose down wing twist is indicated by a nonpositive angle.

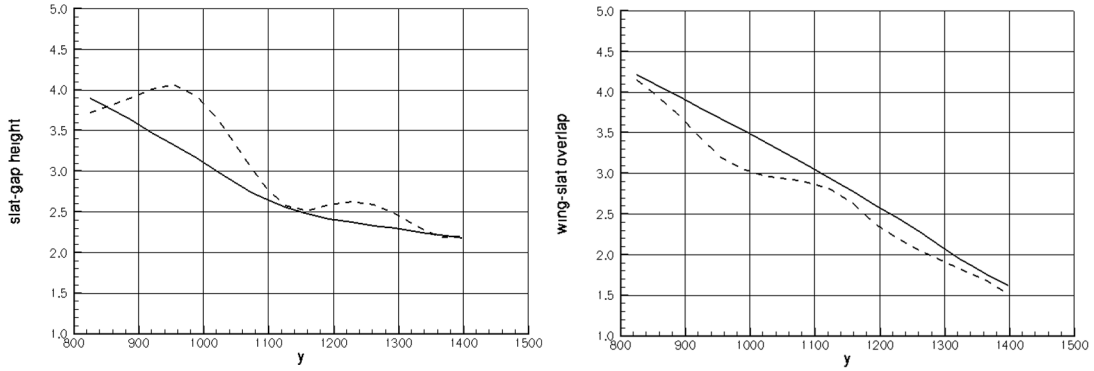

Fig. 26 Computed slat-gap height (in mm) and wing-slat overlap (in mm) in spanwise direction on the rigid grid (solid line) and deformed (dashed line) for method C at angle of attack $\alpha = \alpha_1$.

change in flap gap height is largest at spanwise location $y = 1000$ mm ($\eta = 0.71$), approximately 0.3 mm (7%). At this location the change in overlap is approximately 0.3 mm (4%).

Although the relative changes in slat gap and overlap are relatively quite large the overall effect on local lift is small (see Fig. 23).

VIII. Conclusions

Geometrical installation and deformation effects for a half-model high-lift wing in a wind-tunnel environment are investigated and found to be significant. The inclusion of wind-tunnel walls explains the main difference (in terms of location and slope) between the experimental and the computed forces due to crossflow velocity components caused by the model mounting (in both the LSWT and ETW wind tunnels). The other geometric effects are important, but not as significant. A good understanding is obtained of the influences of the half-model test technique for high-lift models.

The inclusion of additional geometric detail does influence lift and maximum lift. The presence of pressure tube bundles reduces maximum lift and the angle of attack at which maximum lift occurs. Aeroelastic effects are present but seem to be of secondary interest in comparison to the effect of wind-tunnel walls and model mounting. Aeroelastic effects will become more important for larger dynamic pressures (at larger wind-tunnel Reynolds numbers or at the flight conditions).

The modeling of the additional geometric installation and deformation effects comes at an increased computational cost. It is estimated that the extra computational cost for model deformation is about 10%, for including slat tracks and pressure tube bundles it is approximately 10% (depending on the amount of grid resolution introduced), and for including wind-tunnel walls and model mounting it is about 400%. The computational cost to include wind-tunnel walls and model mounting is so large due to the necessity to generate computational viscous grids for the entire wind tunnel, one for each angle of attack, and to set the backpressure to match upstream flow conditions.

The computational time to perform a viscous flow computation for high-lift configuration with a high level of geometrical detail is large. The computational time can be reduced by employing grid stretching in spanwise direction at the leading-edge wing elements. In the aeroelastic loop the computational time can be reduced significantly by applying a highly efficient algebraic tetrahedral grid deformation algorithm.

One of the major lessons learned is that the modeling of additional geometrical details (wind-tunnel walls, model mounting, deformation, slat tracks, bundles) brings numerical results closer to experimental values. It is expected that bringing together all geometric effects leads to a better prediction of experimental lift and drag. This could contribute to the development of enhanced wall correction methods and to the improvement of future experimental results.

Acknowledgment

The authors wish to thank Heinz Jakob (Airbus-Germany) for providing useful contributions, comments, and feedback concerning the content of this paper.

References

[1] van Dam, C. P., "The Aerodynamic Design of Multi-Element High-Lift Systems for Transport Airplanes," *Progress in Aerospace Sciences*, Vol. 38, No. 2, Feb. 2002, pp. 101–144. doi:10.1016/S0376-0421(02)00002-7

[2] Reckzeh, D., "Aerodynamic Design of the High-Lift Wing for a Megaliner Aircraft," *Aerospace Science and Technology*, Vol. 7, No. 2, March 2003, pp. 107–119. doi:10.1016/S1270-9638(02)00002-0

[3] Rudnik, R., "Stall Behaviour of the Eurolift High-Lift Configurations," AIAA Paper 2008-836, 2008.

[4] Rudnik, R., and Germain, E., "Re-No. Scaling Effects on the EUROLIFT High-lift Configurations," AIAA Paper 2007-752, Jan. 2007.

[5] Murayama, M., Yokokawa, Y., and Yamamoto, K., "Validation Study of CFD Analysis for High-Lift Systems," *25th International Congress of the Aeronautical Sciences*, ICAS, Hamburg, Germany, Sept. 2006.

[6] Perraud, J., and Moens, F., "Transport Aircraft 3D High-Lift Wing Numerical Transition Prediction," AIAA Paper 2007-262, Jan. 2007.

[7] Rogers, S. E., Roth, K., Cao, H. V., Slotnick, J. P., Whitlock, M., Nash, S. M., and Baker, M. D., "Computation of Viscous Flow for a Boeing 777 Aircraft in Landing Configuration," *Journal of Aircraft*, Vol. 38, No. 6, 2001, pp. 1060–1068. doi:10.2514/2.2873

[8] von Geyr, H, van der Burg, J. W., Eliasson, P., and Esquieu, S., "CFD Prediction of Maximum Lift Effects on Realistic High-Lift Commercial Aircraft Configurations Within the European Project Eurolift II," AIAA Paper 2007-4299, 2007.

[9] Reckzeh, D., and Hansen, H., "High Reynolds-Number Windtunnel Testing for the Design of Airbus High-Lift Wings," *New Results in Numerical and Experimental Fluid Mechanics V*, Vol. 92, Notes on Numerical Fluid Mechanics and Multidisciplinary Design, Springer, Berlin, 2006, pp. 1–8.

[10] Rudnik, R., "CFD Assessment for 3D High-Lift Flows in European Project Eurolift," AIAA Paper 2003-3794, 2003.

[11] van der Burg, J. W., Maseland, H., and Brandsma, F. J., "Low Speed Maximum Lift and Flow Control," *Aerospace Science and Technology*, Vol. 8, No. 5, 2004, pp. 389–400. doi:10.1016/j.ast.2004.01.004

[12] Eliasson, P., le Pape, M., Ortmann, J., Pelizarri, E., and Ponsin, J., "Improved CFD Predictions for High-Lift Flows in the European Project Eurolift II," AIAA Paper 2007-4303, 2007.

[13] Rumsey, C. L., Lee-Rausch, E. M., and Watson, R. D., "Three-Dimensional Effects on Multi-Element High-Lift Computations," AIAA Paper 2002-0845, 2002.

[14] Rogers, S. E., Roth, K., and Nash, S. M., "Validation of Computed High-Lift Flows with Significant Wind-Tunnel Effects," *AIAA Journal*, Vol. 39, No. 10, 2001, pp. 1884–1892. doi:10.2514/2.1203

[15] Chang, K. C., Chen, H. H., Tzong, T., and Cebeci, T., "Aeroelastic Analysis of High-Lift Configurations," AIAA Paper 2000-0905, 2000.

[16] Burner, A. W., Liu, A., Garg, S., Ghee, T., and Taylor, N., "Aeroelastic Deformation Measurements of Flap, Gap, and Overhang on a Semispan Model," AIAA Paper 2000-2386, June 2000.

[17] van der Burg, J. W., Prananta, B. B., and Soemarwoto, B. I., "Aeroelastic CFD Studies for Geometrically Complex Aircraft Configurations," *Proceedings of the International Forum on Aeroelasticity and Structural Dynamics (IFASD2005)*, IFAS, July 2005 [CD-ROM].

[18] Courty, J.-C., Delille, T., and Dassault Aviation, "Validation of In-Tunnel High-Lift Computations," *Proceedings of European Air and Space Conference (CEAS 2007)*, CEAS, Sept. 2007 [CD-ROM].

[19] Eliasson, P., "Investigation of a Half-Model High-Lift Configuration in a Wind Tunnel," *Journal of Aircraft*, Vol. 45, No. 1, 2008, pp. 29–37. doi:10.2514/1.34054

[20] Gerhold, T., "Efficient Algorithms for Mesh Deformation," *ODAS Symposium*, ODAS, 2006 [CD-ROM].

[21] Liu, X., Qin, N., and Xia, H., "Fast Dynamic Grid Deformation Based on Delaunay Graph Mapping," *Journal of Computational Physics*, Vol. 211, No. 2, Jan. 2006, pp. 405–423. doi:10.1016/j.jcp.2005.05.025

[22] Heinrich, R., Kroll, N., Neumann, N., and Nagel, B., "Fluid-Structure Coupling for Aerodynamic Analysis and Design—A DLR Perspective," AIAA Paper 2008-561, 2008.

[23] van der Burg, J. W., van der Heul, D. R., and Schippers, H., "Unstructured Grid Coarsening for Efficient Analysis of Cavity Backed Stacked Patch Antennas," *Proceedings of the 9th International Conference on Numerical Grid Generation in Computational Field Simulations*, International Society of Grid Generation, Department of Mechanical Engineering, University of Alabama at Birmingham, Birmingham, AL, June 2005; also issued as NLR Technical Publication 2005-193.

[24] van der Burg, J. W. , Maseland, J. E. J., and Oskam, B., "Development of a Fully Automated CFD System for Three-Dimensional Flow Simulations Based on Hybrid Prismatic-Tetrahedral Grids," *Proceedings of the 5th International Conference on Numerical Grid Generation in Computational Field Simulations*, NSF Engineering Research Center for Computational Field Simulation, College of Engineering, Mississippi State University, Mississippi State, MS, April 1996; also issued as NLR Technical Publication 96036U.

[25] Choi, Y. H., and Merkle, C. L., "The Application of Preconditioning in Viscous Flows," *Journal of Computational Physics*, Vol. 105, No. 2, April 1993, pp. 207–223. doi:10.1006/jcph.1993.1069

E. Livne
Associate Editor